

Supporting Information for

Colloidal WSe₂ Nanocrystals as Anodes for Lithium-Ion Batteries

Pengshang Zhou^{ab^}, Gearoid Collins^{c^}, Zeger Hens^{ab}, Kevin M. Ryan^c, Hugh Geaney^{c*} and Shalini Singh^{abc*}

^a *Physics and Chemistry of Nanostructures, Ghent University, 9000 Ghent, Belgium*

^b *Center for Nano and Biophotonics, Ghent University, 9000 Ghent, Belgium*

^c *Department of Chemical Sciences and Bernal Institute, University of Limerick, Limerick, Ireland*

[‡] *These authors have contributed equally to this work.*

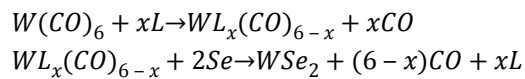
*Corresponding Authors: Hugh.Geaney@ul.ie; Shalini.Singh@ul.ie

Sections

- S1 The reaction mechanism of WSe₂ formation
- S2 XRD spectra of NS-2H and NS-1T'
- S3 Se XPS analysis of the nanosheets sample
- S4 AFM analysis of the nanoflower sample
- S5 Se XPS analysis of the nanoflowers
- S6 XRD analysis of the nanoflowers
- S7 Electrochemical analysis of NF-2H nanoflowers
- S8 Postmortem ex-situ characterization of anode materials
- S9 Rate effect on NF-2H nanoflowers
- S10 Electrolyte effect on NF-2H electrochemical behaviour

S1 The reaction mechanism of WSe₂ formation

The formation mechanism of WSe₂ is supposed to be a two-step process. The oxidation state of W in W(CO)₆ is 0. When W(CO)₆ is heated at high temperature with ligand/solvent, it loses carbonyl either partially or completely in the form of carbon monoxide and may form new complex with the ligand present in the flask. Contrary to this, Se is in elemental form. When it is injected in the flask, it is reduced from 0 to -2 oxidation state upon reaction with the metal complex. The tentative reaction mechanism is given below where L is the ligand used (oleylamine or oleic acid):



It should be noted that here L (ligand) is in excess. After the synthesis, it can form an adduct with the colloidal WSe₂ nanocrystals to passivate the surface as WSe₂.

S2 XRD spectra of NS-2H and NS-1T'

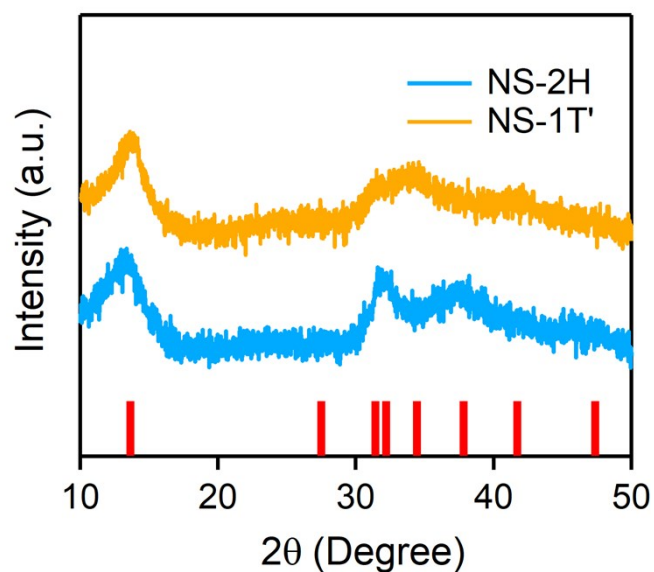


Fig. S1 XRD spectra of NS-2H and NS-1T'. The red sticks at the bottom indicate the positions of WSe₂ crystal from the PDF card #38-1388.

X-ray diffraction (XRD) patterns of both samples are shown in Fig. S1, as we can see from it, NS-2H samples show peaks that are in line with 2H WSe₂ (PDF:38-1388). While for the NS-1T', the XRD show broad peaks with most of the intensity lost in the background due to the low-crystallinity of NS-1T'. This is a common issue in the colloidal 1T' structure occurring due the low-crystallinity of the synthesized samples.

S3 Se XPS analysis of the nanosheets sample

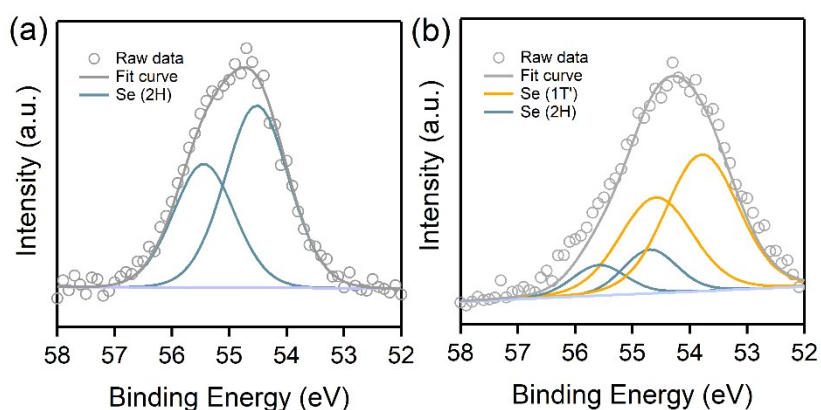


Fig. S2 High resolution Se XPS spectra recorded from NS-2H and NS-1T', respectively.

In order to further demonstrate the phase composition, Se 3d analysis of both nanosheets samples were performed. As shown in Fig. S2a, only one type of S^{2-} atom is found in NS-2H, which suggests only one phase appear in NS-2H, and the positions of the peaks indicate it is 2H phase. While for NS-1T' (Fig. S2b), the Se core level electrons was fitted with four doublets, the accurate peak values are shown in Table S2.

Table S1. XPS peak positions (in eV) obtained after deconvolution of W region of the nanosheets.

Sample	1T'		2H		W (IV)		W 5p
	W 4f _{7/2}	W 4f _{5/2}	W 4f _{7/2}	W 4f _{5/2}	W 4f _{7/2}	W 4f _{5/2}	
NS-2H	-	-	32.32	34.42	35.64	37.94	36.90
NS-1T'	31.70	33.80	32.51	34.61	35.75	37.85	36.90

Table S2. XPS peak positions (in eV) obtained after deconvolution of Se region of the nanosheets.

Sample	1T'		2H	
	Se 3d _{5/2}	Se 3d _{3/2}	Se 3d _{5/2}	Se 3d _{3/2}
NS-2H	-	-	54.58	55.54
NS-1T'	53.78	54.58	54.69	55.58

S4 AFM analysis of the nanoflower sample

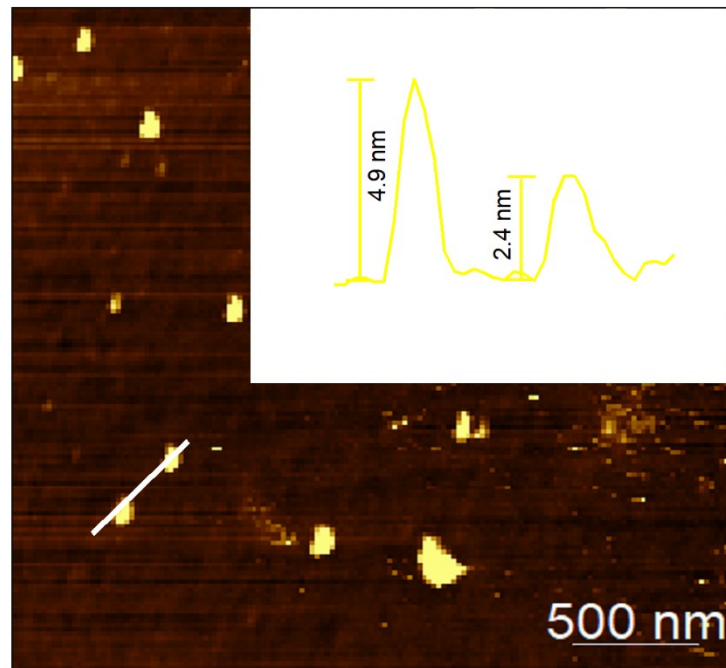


Fig. S3 AFM of the NF-2H. Insert: The height profile of the white line.

AFM was carried out to check the thickness of the nanoflower sample. The height profile shown insert (Fig. S3) reveals the thickness of the nanoflower layers to be in the range of 2.4-4.9 nm, which correspond to 4 and 7-layer.

S5 Se XPS analysis of the nanoflowers

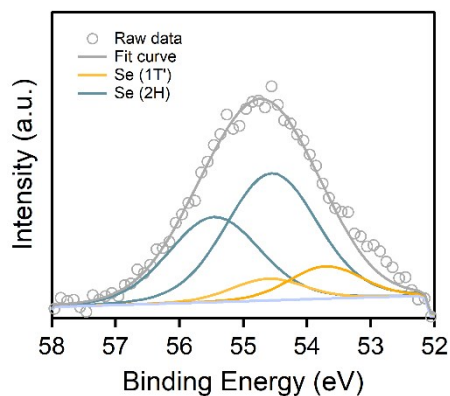


Fig. S4 XPS of Se signals recorded from NF-2H sample.

Fig. S4 displays the Se signals analysis of the nanoflower sample. As we can see from it, the spectra is dominated by two strong peaks around 54.6 eV and 55.5 eV, which correspond to Se $3d_{5/2}$ and Se $3d_{3/2}$ of 2H WSe_2 .¹⁻³ Moreover, the appearance of peaks at lower binding energies indicate the existence of a small amount of 1T' phase. Table S3 clearly shows the positions of the peaks in Fig. 4b and Fig. S4.

Table S3. XPS peak positions (in eV) obtained after deconvolution of W and Se region of the nanoflowers.

	W		Se	
1T'	31.65	33.75	53.51	54.40
2H	32.42	34.52	54.55	55.45
W (VI)	35.83	38.03		
W 5p	36.87			

S6 XRD analysis of the nanoflowers

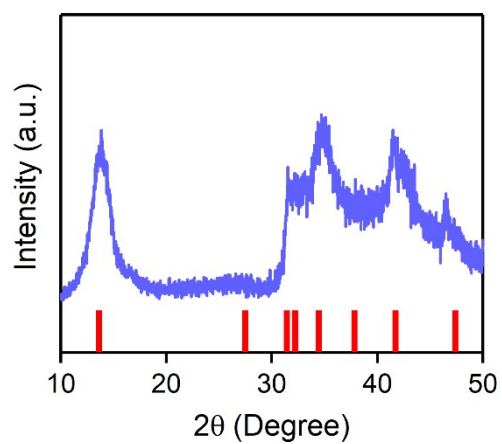


Fig. S5 XRD spectra of the NF-2H sample. The red sticks at the bottom indicate the positions of WSe₂ crystal from the PDF card #38-1388.

XRD of the NF-2H sample is shown in Fig. S5. The positions of the peaks are in good accordance with 2H WSe₂ (PDF:38-1388).

S7 Electrochemical Analysis of NF-2H Nanoflowers

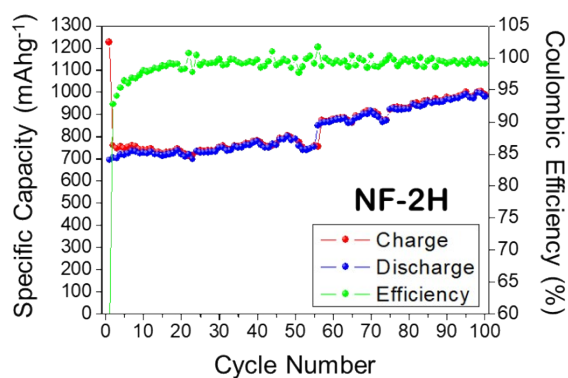


Fig. S6 Charge/discharge ageing of NF-2H. This data corresponds with the data in figure 5a. The cell was cycled at 100 mA g^{-1} between 0.01-3.0 V vs Li/Li⁺.

NF-2H anodes demonstrate high capacity and excellent stability and reversibility in Li metal half-cells, with an average coulombic efficiency of 99.84 % and no capacity fade over 100 cycles.

S8 Postmortem ex-situ characterization of anode materials

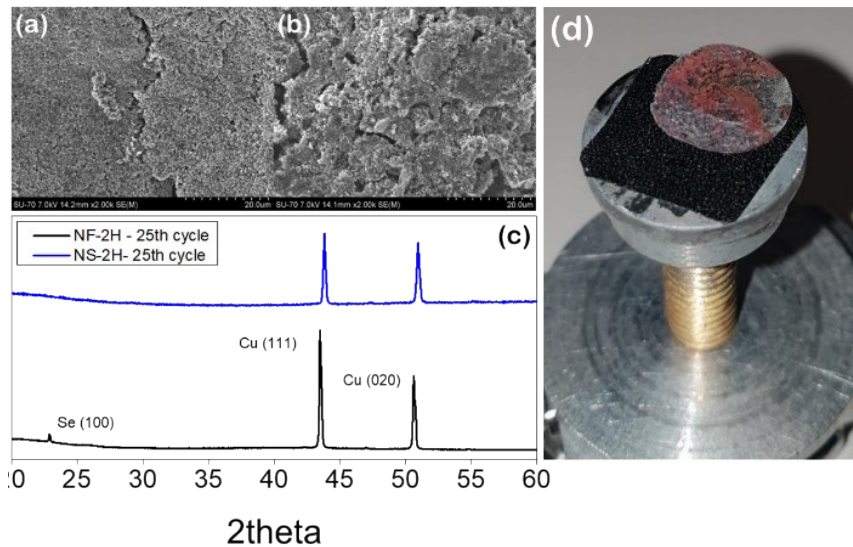


Fig. S7. Low magnification SEM images of (a) sample 1 and (b) sample 3, cycled for 24 cycles followed by low current slow charge to 0.01 V. (c) Stacked X-ray diffraction patterns of WSe_2 anodes after the 25th charge cycle at a current rate of 100mA g^{-1} . The large peaks at 43.48° and 50.63° correspond to elemental copper [JCPDS card no. 04-0836] and the peak at 22.67° is in good agreement with elemental selenium [JCPDS card No. 06-0362]. (d) Image of NF-2H take after cycling. The red tinge is characteristic of elemental selenium formation.

To better understand differences in electrochemical performance between NS-2H and NF-2H polymorphs, SEM and XRD were employed to track variations in surface morphology and crystal structure with cycling (Fig. S7). Low magnification SEM images of the cycled anodes did not reveal any major differences in structural morphology (Fig. S7a and b). Both anodes remain well adhered to the underlying copper substrate, suggesting that capacity fade of NS-2H is not attributable to the loss of active material through pulverisation or delamination effects. XRD was employed to track changes in the crystalline structure of WSe_2 with cycling, uncovering a distinct peak associated with crystalline selenium in NF-2H (Fig. S7c). Cell capacity is largely dictated by the availability of selenium for alloying with lithium. Consequently, increased selenium precipitation increases total cell capacity through lithium-selenium side reactions.^{4, 5}

XRD of the anodes, taken after the 25th charge revealed the presence of elemental selenium in NF-2H. In Fig. S7c, a distinct peak emerges after 25 cycles at 22.67 degree, corresponding to Se (100). Continual cycling liberates selenium from the anode, undergoing lithiation in successive cycles to further increase cell capacity through reversible lithium selenide reactions. Fig. S7d verifies this characteristic selenium liberation, with the red discolouration of the anode, characteristic of elemental selenium.⁶ A similar process was noticed by Yang et al., whereby Na_2Se precipitates elemental Se through oxidation of the sodiated state.⁷ Similarly, Sen et al. noted the evolution of elemental sulfur during cycling, undergoing side

reactions forming lithium sulfides.⁸ XRD analysis of post-cycled WSe_2 anodes demonstrated similar evolution of elemental selenium from the layered structure, analogous to sulfur liberation in MoS_2 -derived systems. An analogous behaviour was noted by Zhang et al. in $MoSe_2$ nanosheets, attributing increased cell capacity to the precipitation of elemental selenium to undergo side reactions, forming selenides.⁴

S9 Rate Effect on NF-2H Nanoflowers

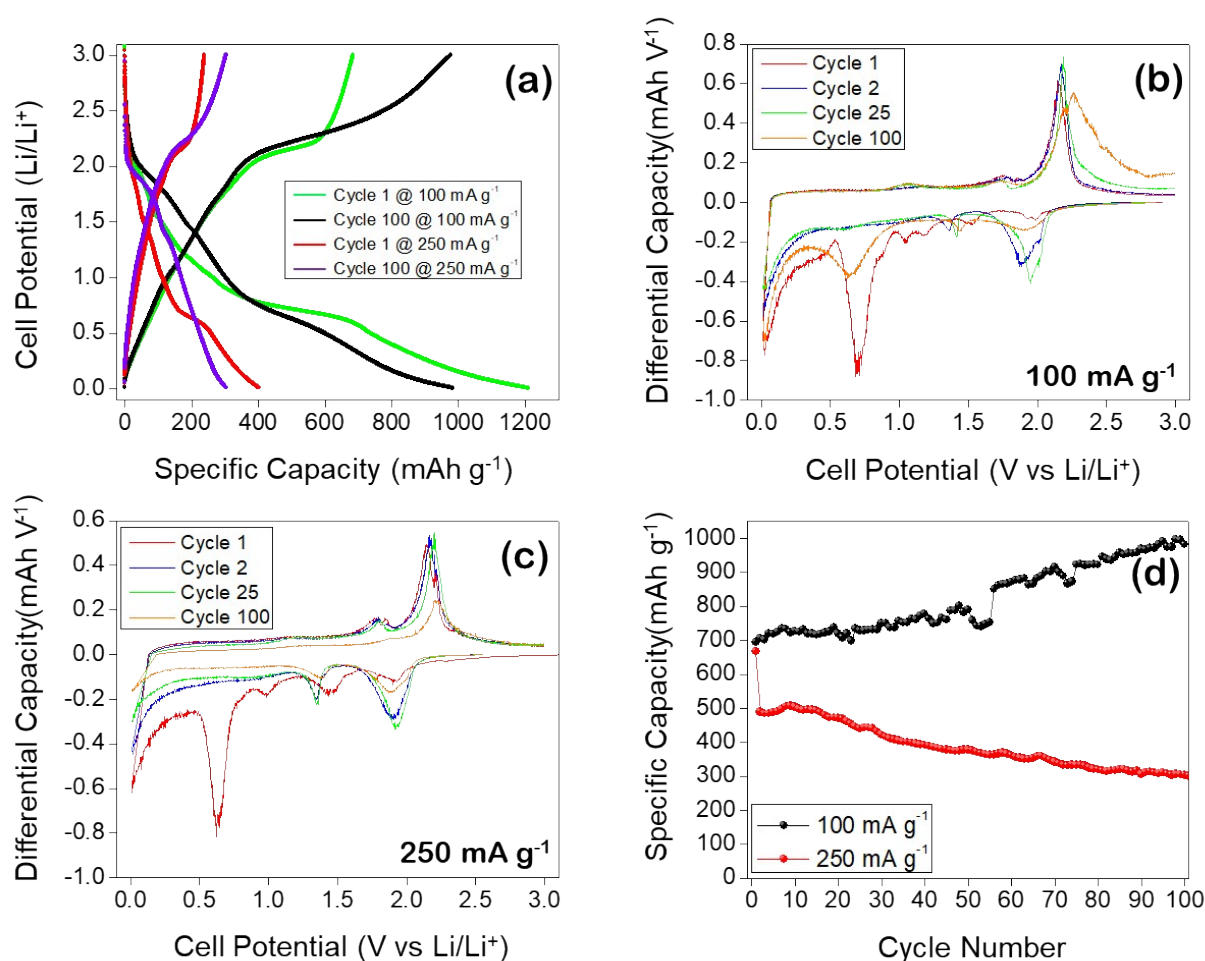


Fig. S8: Electrochemical analysis of the effect of applied current density on the lithiation/delithiation behaviour of NF-2H. (a) capacity profiles for the 1st and 100th cycles of NF-2H @ 100 mA g⁻¹ and 250 mA g⁻¹, and DCPs of the 1st (red), 2nd (blue), 25th (green) and 100th (orange) cycle of Li || NF-2H HCs at (b) 100 mA g⁻¹ and (c) 250 mA g⁻¹.

To determine the effect of current density on the lithiation/delithiation behaviour of NF-2H, two comparable Li || NF-2H cells were cycled at 100 mA g⁻¹ and 250 mA g⁻¹ (Fig.S8). Interestingly, the major NF-2H lithiation plateau (0.67 V) that appears after 100 cycles @ 100 mA g⁻¹ is not observed after 100 cycles @ 250 mA g⁻¹ (Fig. S8a), suggesting that slower deep lithiation is required to displace metallic Se from WSe₂. This is reflected by the emergence of a major cathodic peak at 0.67 V after 100 cycles at 100 mA g⁻¹ (Fig. S8b). A comparable rise in the delithiation peak at 1.06 V for NF-2H at 100 mA g⁻¹ (Fig. S8b) is not observed after 100 cycles at 250 mA g⁻¹ (Fig. S8c), suggesting a coupling of these redox peaks. Notably, at both rates, the cycling behaviour of NF-2H is dictated by an overarching two-step intercalation-

conversion process, forming the intermediate Li_xWSe_2 via intercalation at ~ 2 V which converts to W and Li_2Se at lower voltages. During delithiation, the intermediate Li_xWSe_2 is formed (~ 1.8 V) followed by deintercalation to reform WSe_2 to some degree (~ 2.2 V). At 100 mA g^{-1} , the gradual formation of metallic Se at the anode surface sees a gradual increase in specific capacity. For $\text{Li} | \text{NF-2H}$ cycled at 250 mA g^{-1} , this gradual precipitation of Se is not observed over the 1st 100 cycles, with 100 mAh g and 250 mA g cell capacities differing by 685 mAh g^{-1} after 100 cycles (Fig. S8d).

S10 Electrolyte Effect on NF-2H Electrochemical Behaviour

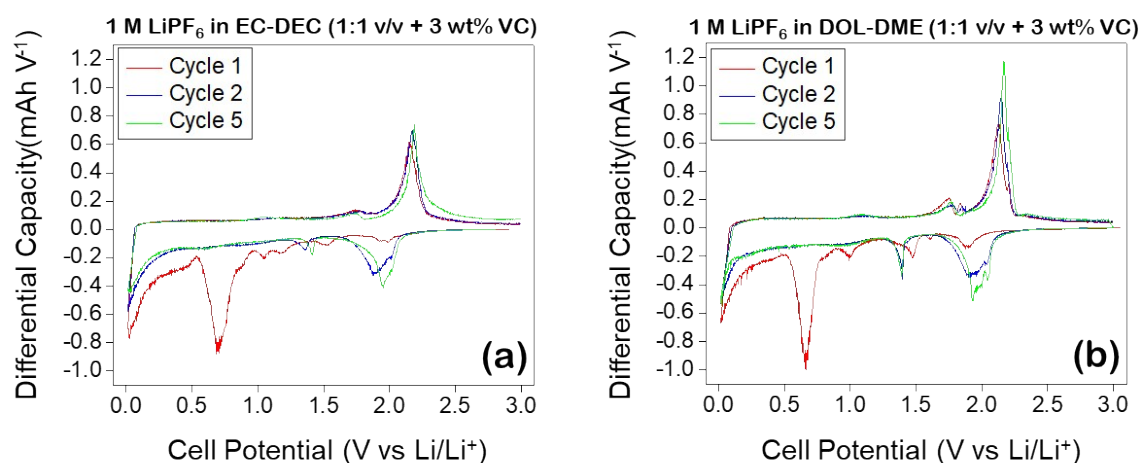


Fig. S9: Electrochemical analysis of the effect of electrolyte on the lithiation/delithiation behaviour of NF-2H. (a) DCPs of Li | NF-2H HC in a 1 M LiPF₆ in EC-DEC (1:1 v/v) solution for the 1st (red), 2nd (blue), 25th (green) and 100th (orange) cycle and a of Li | NF-2H HC in a (b) 1 M LiTFSI in DOL-DME (1:1 v/v) solution for the 1st (red), 2nd (blue) and 5th (green) and cycle. Both cells were cycled with an applied current density of 100 mA g⁻¹.

Li-Se cathode systems have demonstrated an electrolyte-dependent multi-phase lithiation of pure Se.⁷⁻¹⁰ Eftekhari noted that Se lithiation in analogous Li-Se battery systems is dictated by electrolyte composition.⁷ Ether-based solvents promoted multiple intermediate Li_xSe phases whereas carbonate solvents allowed for only a single-step Li-Se alloying process. The effect of electrolyte on the lithiation behaviour of NF-2H WSe₂ anodes was analysed through constant current ageing (100 mA g⁻¹) of Li | NF-2H cells in a 1 M LiPF₆ in EC-DEC + 3 wt% VC vs a 1 M LiPF₆ in DOL-DME. Li | NF-2H cells tested in a carbonate-based (Fig. S9a) electrolyte (1 M LiPF₆ in EC-DEC (1:1 v/v)) and an ether-based (Fig. S9b) electrolyte (1 M LiPF₆ in EC-DEC (1:1 v/v)) demonstrated near identical lithiation/delithiation behaviours over the first 5 cycles, with capacity contributions arising from intercalation, Li_xWSe₂ formation, conversion to W and Li₂Se along with W pseudocapacitance. Notably, NF-2H is governed by a two-step intercalation conversion lithiation/delithiation process, irrespective of electrolyte composition. The electrolyte-specific multi-phase alloying process of analogous Li-selenide battery systems was not observed for WSe₂, suggesting an electrolyte-independent lithiation/delithiation behaviour of WSe₂.

References

1. J. Guo, Y. Shi, X. Bai, X. Wang and T. Ma, *Journal of Materials Chemistry A*, 2015, **3**, 24397-24404.
2. G. Zhang, X. Zheng, Q. Xu, J. Zhang, W. Liu and J. Chen, *Journal of Materials Chemistry A*, 2018, **6**, 4793-4800.
3. M. S. Sokolikova, P. C. Sherrell, P. Palczynski, V. L. Bemmer and C. Mattevi, *Nat Commun*, 2019, **10**, 712.
4. H.-J. Zhang, Y.-K. Wang and L.-B. Kong, *Nanoscale*, 2019, **11**, 7263-7276.
5. J. Ge, L. Fan, J. Wang, Q. Zhang, Z. Liu, E. Zhang, Q. Liu, X. Yu and B. Lu, *Advanced Energy Materials*, 2018, **8**, 1801477.
6. C. G. Wilber, *Clinical Toxicology*, 1980, **17**, 171-230.
7. W. Yang, J. Wang, C. Si, Z. Peng and Z. Zhang, *Nano Research*, 2017, **10**, 2584-2598.
8. U. K. Sen and S. Mitra, *ACS Applied Materials & Interfaces*, 2013, **5**, 1240-1247.